Journal of Power Sources
Volume 541, 1 September 2022, 231644

Strong ion pairing at the origin of modified Li-cation solvation and improved performances of dual-salt electrolytes

Xiaozhe Zhang [a], Xiaodong Lin [a], Pan Xu [b], Ruming Yuan [b], Deepak Gupta [a], Rico Rupp [a], Gabriella Barozzino-Consiglio [a], Hewei Xu [a], Quanfeng Dong [b], Alexandru Vlad [a]

DOI : 10.1016/j.jpowsour.2022.231644

Strong Ion Pairing at the Origin of Modified Li-cation Solvation and Improved Performances of Dual-salt Electrolytes

Xiaozhe Zhang[a], Xiaodong Lin[a], Pan Xu[b], Ruming Yuan[b], Deepak Gupta[a], Rico Rupp[a], Gabriella Barozzino-Consiglio[a], Hewei Xu[a], Quanfeng Dong[b], and Alexandru Vlad*[a]

[a.] Institute of Condensed Matter and Nanosciences, Université catholique de Louvain, Louvain-la-Neuve, Belgium.

[b.] Collaborative Innovation Centre of Chemistry for Energy Materials (iChEM), State Key Laboratory of Physical Chemistry of Solid Surfaces, Department of Chemistry, College of Chemistry and Chemical Engineering, Engineering Research Centre of Electrochemical Technologies of Ministry of Education, Xiamen University. Xiamen 361005, China.

E-mail: alexandru.vlad@uclouvain.be

ABSTRACT: Organic phosphates have been widely used as fire-retardant additives or co-solvents to improve the safety of Li-ion electrolytes. However, these solvents show poor compatibility with low potential electrodes and cannot work efficiently as sole solvent and at low salt concentration. The utilization of high concentration electrolytes was shown to improve the interfacial properties by altering the solvation structure but the drawbacks are low ionic conductivity, high viscosity, and elevated costs. Herein, a dual-salt phosphate-based electrolyte consisting of medium concentration Lithium nitrate ($LiNO_3$) and Lithium bis(trifluoromethanesulfonyl)imide (LiTFSI) salts in triethyl phosphate (TEP) is analyzed and found to address the above issues. Benefiting from the strong affinity between NO_3^- and Li^+, the use of $LiNO_3$ is found to perturb the solvation structure, with mixed anion (NO_3^- and $TFSI^-$) pairing with Li^+. The detailed environment of Li^+ in dual-salt phosphate-based electrolyte is probed through nuclear magnetic resonance and Raman analysis, corroborated by density functional theory calculations. The dual-salt formulation is found to lead to the formation of a LiF-Li_3N-LiN_xO_y-rich solid-electrolyte interphase on Lithium metal electrode surface. The results and analyses not only allow the assembly of $LiNi_{0.5}Co_{0.2}Mn_{0.3}O_2$||Li cells with significantly improved cycling and low temperature performances but also shine light on taming strong polarity phosphate electrolytes with fine solvation interplay.

Keywords: Li-metal batteries, dual-salt electrolyte, solvation structure, ion pairing, solid-electrolyte interphase

1. Introduction

In the past few decades, rechargeable Li-ion batteries (LIBs) have witnessed rapid developments and become an essential part of our life.[1-4] However, their further application in large-scale devices, such as electric vehicles, is impeded by safety issues resulting from the use of highly flammable and volatile organic carbonates as electrolyte solvents.[5, 6] In this context, non-flammable compounds such as organic phosphates,[7-9] ionic liquids,[10-13] and fluorinated ethers/esters,[14-16] have been employed as additive, co-solvent, or as sole solvent for electrolytes to improve the safety characteristics of LIBs. Among these, organic phosphate solvents have attracted considerable attention due to their intrinsic fire-retardant ability, low cost and suitable physicochemical properties as electrolyte solvent, as for example their capacity to dissolve large amount of salt (e.g., ~5.8 M LiFSI dissolved in triethyl phosphate).[17] However, organic phosphates are unable to generate a stable solid-electrolyte interphase (SEI) on the anode electrode surface (e.g., graphite, silicon, Li/Na metal) since a solvent-derived SEI is primarily formed (presumably porous, permeable or partially soluble), which results in poor electrochemical performance.[18-21]

Recent studies have shown that increasing the salt concentration can overcome the above mentioned issues.[22] The threshold is generally found around 3 M,[6] wherein the salt-to-solvent molar ratio is ≥ 1:2, as all (or most) solvent molecules are confined in the primary Li-cation solvation shell [17]. This results in solvent stabilization and

kinetically favors the formation of anion-derived SEI, resulting in improved electrode interphases and cycling performances. However, the use of high concentration electrolytes comes along with the disadvantages of low ionic conductivity, high viscosity, poor electrode and separator wetting, as well as high costs.[23-25] Therefore, to promote the practical application of phosphate-based electrolyte, it is essential to develop phosphate-based electrolyte formulations that can surmount the shortcomings of the high concentration systems while maintain its advantages.

$LiNO_3$ has been extensively applied as additive in various electrolyte systems and demonstrated to be effective in stabilizing the Li metal surface by forming passivating nitride rich SEI.[25-27] For example, Zhang and his coworkers reported that the addition of $LiNO_3$ altered the solvation structure of Li-cations in a bis(fluorosulfonyl)imide (FSI^-) – 1,2-dimethoxyethane (DME) based electrolyte system, thus facilitating complete decomposition of anions and forming a robust anion-derived SEI on Li metal anode.[28] Fu and coworkers also demonstrated that NO_3^- can participate in the solvation sheath of Li-cations in sulfone-based electrolytes leading to the formation of a stable LiF-Li_3N-LiN_xO_y-rich SEI on Li metal surface.[29] Despite the reported effects of $LiNO_3$ additive in various electrolytes, its application in phosphate-based electrolytes (especially in dual-salt formulations) remains scarcely reported and the role of nitrate in Li^+ solvation structure change is seldomly addressed.

Inspired by the positive effect of $LiNO_3$ additive in the various electrolyte systems, in this work we study the effect of $LiNO_3$ used as co-salt in a LiTFSI/TEP electrolyte formulation. The $LiNO_3$-LiTFSI/TEP dual-salt electrolyte is shown to improve the compatibility of phosphate-based electrolyte with Li metal anode at a medium concentration of 3 M in total Li-cations. A series of experimental and theoretical analyses reveal the role of $LiNO_3$ in modulating the solvation structure of Li-cations by pairing with $TFSI^-$ /NO_3^- anions in the solvation shell (Figure 1a). A particular solvation structure is found, that is considered to promote the formation of an anion-derived SEI consisting of primarily inorganic species, e.g., LiF, Li_3N and LiN_xO_y, etc. This thus is found to effectively enhance the interfacial stability of phosphate-based electrolytes at Li metal anode surface. As a result, the $LiNi_{0.5}Co_{0.2}Mn_{0.3}O_2$||Li cells with the dual-salt electrolyte are found to display improved rate capability at also low temperature performances.

2. Experimental Section

2.1. Chemicals and Materials

Li metal chips, coin cell assembly parts (stainless steel, SS-316), $LiNi_{0.5}Co_{0.2}Mn_{0.3}O_2$ (NCM523), conductive carbon and poly (vinylidene difluoride) (PVDF) were purchased from TOB new energy technology Co., Ltd. (Xiamen, China). Glass fiber separator (GF/D) was purchased from Whatman. Triethyl phosphate (TEP,

Battery Grade, Fluorochem Co., Ltd.) was chosen as electrolyte solvent and used after drying over molecular sieves (4 Å, Sigma-Aldrich) to ensure a water content of less than 5 ppm (determined by Karl Fischer titration, Metrohm 899 Coulometer). LiTFSI (battery grade, DoDochem) and $LiNO_3$ (anhydrous, 99%, Alfa Aesar) were dried under vacuum at 100 °C for 12 hours in an argon-filled glovebox before use.

2.2. Battery Assembly and Electrochemical Measurements

The NCM cathode was prepared by mixing NCM523 powder, conductive carbon and PVDF binder in a weight ratio of 85:8:7 in N-methyl-2-pyrrolidinone (NMP) to form a homogeneous slurry. The slurry was coated on Al foil and dried at 120 °C under dynamic vacuum overnight. Afterwards, circular electrodes of 12 mm in diameter were cut, pressed, dried for 12 hours at 120 °C in vacuum oven and weighted. The mass loading of NCM523 electrodes was in the range of 5.0−5.5 mg cm^{-2}. CR2032-type coin cells were assembled with a Li metal foil as counter and pseudo-reference electrode, one sheet of glass fiber as a separator soaked with the selected electrolyte (120~150 μl), and one NCM sheet as working electrode in an argon-filled glovebox (MBraun, Inc., H_2O < 1 ppm, O_2 < 1 ppm). The galvanostatic charge−discharge tests were performed on Neware battery testing system (Shenzhen Neware Electron. Co. Ltd., China) within the potential range of 3.0−4.5 V (vs. Li/Li^+). The specific capacity and current density were calculated based on the mass of NCM523.

The ionic conductivity of studied electrolyte formulations was measured by AC impedance spectroscopy using an SP300 potentiostat (Biologic). A polypropylene gasket with an internal diameter of 11.3 mm and outer diameter of 16.4 mm was specially designed and made using a 3D-printer (Ultimaker 3) and placed in between the two stainless steel disks inside a CR2032 coin cell. The cell was filled with electrolyte, and the contact between the disks and the gasket was ensured by a metallic spring. The ionic conductivity of the electrolyte was calculated according to the equation: $C=L/(R\cdot A)$; where R is the resistance of the electrolyte (as estimated from EIS plots), L is the separation between the two metal plate electrodes (0.6 mm), and A is the contact area (1 cm^2).

Symmetric Li||Li coin cells were also assembled to study the lithium stripping/deposition and the cycling behavior on lithium metal substrate. A gasket with an internal area of 0.5 cm^2 was cut from 45 μm thick high-density polyethylene (HDPE) foil (Scancell Folien-Vertriebs GmbH) and placed on top of the lithium metal electrode. A stainless steel (SS-316) disc and spring were added on top of the lithium chip to guarantee uniform pressure. The cell was then crimped inside a CR2032 coin cell case (SS-316). The galvanostatic charge−discharge tests were performed on a Neware battery testing system (Shenzhen Neware Electron. Co. Ltd., China) after a resting period of 12 h to allow complete wetting of the electrodes and the separator.

2.3. Physico-chemical characterization

X-ray photoelectron spectroscopy (XPS) measurements were performed on a Thermo Scientific Escalab 250Xi$^+$ spectrometer with monochromatized and micro-focused Al Kα X-ray source. The samples were transferred using a special transfer chamber with no exposure to ambient air. Raman spectra were recorded on an NRS-5100 spectrometer (JASCO INTERNATIONAL CO., LTD) with an excitation wavelength of 532 nm. Nuclear magnetic resonance (NMR) spectra were recorded at room temperature (295 K) on a Bruker Avance 500 spectrometer operating at a field strength of 11.7 T (Larmour frequencies of 500.13 MHz for ^{1}H, 202.46 MHz for ^{31}P, 125.76 MHz for ^{13}C and 194.37 MHz for ^{7}Li) using a directly detecting broadband observe (BBO) probe. The ^{1}H and ^{13}C chemical shifts were referenced to the residual C_6HD_5 signal (7.16 ppm) and the C_6D_6 signal (128.06 ppm), respectively. The ^{31}P and ^{7}Li NMR spectra were externally calibrated. The electrolyte samples for NMR measurements were placed into 5 mm NMR tubes in which an external coaxial insert containing 0.15 mL of deuterated benzene (C_6D_6) was introduced. The tubes were sealed in an Ar-filled glovebox to avoid air or moisture contamination in the samples. The surface morphology of the Li metal anode was investigated using field emission scanning electron microscopy (FESEM, HITACHI S-4800), with a short exposure of samples to ambient air during transfer (less than 10 seconds). Thermogravimetric analysis - Differential scanning calorimetry - Mass Spec (TGA-DSC-MS) was

performed with N_2 as carrier gas at a heating rate of 10 °C min^{-1} on a Mettler Toledo TGA/DSC 3+ STARe System, using alumina containers. The viscosity tests for electrolytes were using a DHR-2 dynamic shear rheometer ((Discovery Hybrid Rheometer, 2019, TA Instruments, New Castle, DE, USA).

2.4. Computational Details

ωB97XD functional theory calculations were carried for the analysis of the electrolyte solvation structure. Herein, for N, F, S, O and P, a 6-311+G (d) basis set was adopted, while C, H, Li atoms were described with the 6-31G(d, p) basis set. In addition, the polarizable continuum model (IEFPCM) was chosen to account for the solvent effect with triethyl phosphate solvent, corresponding to the experimental electrolyte environment. To reduce the overestimation of the entropy contribution, we employed a correction of −2.6 (or 2.6) kcal mol^{-1} for 2:1 (or 1:2). All calculations were carried out with the Gaussian 09 program.

3. Results and Discussion

3.1. Solvation structure

The solvation structure has an essential role on bulk electrolyte properties and SEI formation, parameters affecting the overall battery performances. Therefore, we have first investigated the solvent-cation-anions interactions in the $LiNO_3$-LiTFSI binary salt system with TEP solvent. Figures 1b−d and Figures S1−S4 resume the data on optimized solvation structures of the electrolytes containing different concentrations of LiTFSI and/or $LiNO_3$ in TEP as solvent. Specifically, in 1 M LiTFSI-TEP (corresponding to a molar ratio of approximately LiTFSI:TEP = 1:6) system, three solvation structures with comparable stability, and namely 2TEP-Li-TFSI (−7.68 kcal mol^{-1}), 3TEP-Li-TFSI (−8.93 kcal mol^{-1}) and $(4TEP\text{-}Li)^{+}\cdots TFSI^{-}$ (−7.52 kcal mol^{-1}) coexist along with free TEP molecules (Figure S1). For the 2 M LiTFSI-TEP system (LiTFSI:TEP = 1:3 molar ratio) system, the co-existence of same species is found, with the major difference that the amount of free TEP molecules is significantly reduced (Figure S2). Further concentration increase to 3 M LiTFSI (corresponding to a molar ratio of LiTFSI:TEP = 1:2) is marked by major changes with mainly 2TEP-Li-TFSI species found in the system (Figure 1b and Figure S3).

In the $LiNO_3$-TEP system, the strong affinity of NO_3^- towards Li^+ displaces the otherwise strongly solvating TEP molecules from the primary solvation shell leading to the presence of mainly 4TEP-2Li-2NO_3 aggregates (−11.29 kcal mol^{-1}, Figures 1c

and S4). The combination of $LiNO_3$ and LiTFSI leads to additional exotic solvates, and for the selected 1 M LiTFSI with 2 M $LiNO_3$ in TEP electrolyte, an unusual aggregate of 5TEP-3Li-2NO_3-TFSI (−20.53 kcal mol^{-1}, Figure 1d) is found as being the most stable. The anion screening induces weaker Li^+-TEP interaction when compared to the 3 M LiTFSI-TEP formulation, while increasing the anion:TEP ratio within the solvation shell as compared to both, 3 M $LiNO_3$-TEP and 3 M LiTFSI-TEP compositions (Figure 1a).

To consolidate the theoretical model predictions, a series of analytical techniques was employed to study the solvation states in the studied electrolytes. NMR spectroscopy and Raman spectroscopy were used for analyses the Li^+ solvation structure change in different electrolytes. In the ^{31}P NMR spectra (Figure 2a), the pure TEP solvent exhibits only one sharp peak at 0.11 ppm, implying similar environment for all P atoms. Increasing the salt concentration (from 1 M to 3 M for both LiTFSI and $LiNO_3$) results in a ^{31}P NMR signal upfield shift due to the greater d-orbital occupancy effect in the P−O bonds when Li^+ is coordinated by the phosphate molecules, as already observed in a previous study.[30] Note that only a single time-averaged resonance is observed by NMR measurements owing to the fast exchange of solvent coordinated to the Li-cation with uncoordinated solvent on the NMR time-scale.

At 1 M LiTFSI, the NMR spectrum highlights a broad signal indicating the presence of different P-containing species in similar proportions, which are also in slow

equilibrium with each other with respect to the NMR time-scale (contrarily, only one narrow peak would be observed). Increasing the salt concentration provides a less broad peak that can be ascribed to the existence of predominant species in solution, most likely contact ion pairs and/or ions aggregates, which is consistent with both the literature data[31] and our computational results (refer to Figure 1). In contrast, $LiNO_3$ solutions show solely ^{31}P NMR narrow singlets. Assuming, as in the case of LiTFSI electrolyte, that no rapid equilibria between the various co-existing Li^+ solvation structures occur, such a result implies that regardless of the concentration only one main specie is present. As previously noted,[32] $LiNO_3$ shows a higher Lewis basicity than LiTFSI (quantified by the Gutmann donor number of 22.2 kcal mol^{-1} for NO_3^-, whereas it is of only 11.2 kcal mol^{-1} for $TFSI^-$) which suggests a strong NO_3^- association to Li^+ and hence a high propensity for contact ion pair (CIP) formation even at low salt concentrations, as discussed earlier in the computational analysis. As a result, the ^{31}P chemical shift trend observed is based exclusively on the different content of free TEP molecules and not on a structural variation of the Li^+ solvation shell, resulting therefore in a ^{31}P peak upfield shift as the $LiNO_3$ concentration increases. Noteworthy is also the ^{31}P resonance of the 1 M LiTFSI-2 M $LiNO_3$-TEP electrolyte at −1.42 ppm, which represents an intermediated value between the NMR resonances of the LiTFSI and $LiNO_3$ solutions. Although no general conclusions can be drawn, this result proves the

generation of a different species from those already described for both 3 M LiTFSI and $LiNO_3$.

Concerning the ^7Li NMR (Figure S5), the slight upfield shift of the ^7Li signal in the LiTFSI solution reveals a strong interaction between the $TFSI^-$ anions with the Li^+ cations that occurs when a CIP between Li^+ and $TFSI^-$ is formed in the solution due to the increase in electronic density around the Li^+ solvation shell. In contrast, a downfield shift of the ^7Li NMR signal is observed when increasing the $LiNO_3$ concentration from 1 M to 3 M. The dependence on the salt concentration of ^7Li chemical shift further confirms that NO_3^- plays an active role in solvation environment, hence $LiNO_3$-based solutions generate CIP solvate or aggregate structures. Increasing the concentration of NO_3^- increases the number of nitrate anions interacting with any particular Li^+ with respect to TEP, which in turn leads to a downshift of the ^7Li frequency. Whereas coordination of anions to Li^+ would suggest a reverse trend, the observed de-shielding may be reasoned as a combination of the nitrate anion anisotropic effect[33] and the delocalization of the negative charge between the oxygen atoms of NO_3^-.

The ^7Li resonance of the 1 M LiTFSI-2 M $LiNO_3$-TEP electrolyte at −0.02 ppm, located in-between the NMR resonances of the LiTFSI and $LiNO_3$ solutions (as for the ^{31}P NMR signal), can be thus attributed to a possible new Li^+-solvated structure. The ^7Li NMR position indeed proves that both TEP and the $TFSI^-$ and NO_3^- anions participate to the Li^+ solvation shell, as also described for other LiTFSI/$LiNO_3$ dual salt

systems.[32] Therefore, even if NMR data do not provide an incontrovertible proof about the solvation structure, we can reasonably conclude that the NMR chemical shift of ^{7}Li and ^{31}P is in good agreement with a possible formation of an aggregate such as the one shown in Figure 1d.

Additional hints on the solvation structure are further provided by pulsed-field gradient (PFG) NMR analysis of the various LiTFSI and $LiNO_3$ solutions, and compared to the dual-salt 1 M LiTFSI-2 M $LiNO_3$ TEP electrolyte. As presented in Figure S6, the self-diffusion coefficient (calculated based on the results of Figures S7, S8 and S9) of the Li^+ ions (D_{Li+}) and TEP (D_{1H} and D_{31P}) decrease significantly in both LiTFSI-TEP and $LiNO_3$-TEP systems when the concentration of Li^+ is increased from 1 M to 3 M, ascribed to the increased proportion of ions aggregates. The 1 M LiTFSI-2 M $LiNO_3$-TEP formulation nevertheless exhibits the highest diffusion coefficient for both, Li^+ and TEP, amongst the 3 M compositions (3 M $LiNO_3$ or 3 M LiTFSI in TEP). The high diffusion coefficient for the dual salt system when compared to parent 3 M formulations is attributed to the unusual Li^+ solvation structure, with both anions (NO_3^- and $TFSI^-$) pairing with Li^+ in the solvation shell. It has been suggested that the Li ions in the high concentration electrolytes can be transferred from one site to another via a hopping mechanism through the different binding sites, similar to the Li ion transport mechanisms in inorganic solid electrolyte.[29, 34] Thus, benefiting from enhanced and increased Li^+-anion binding sites hopping transport, the anion pairing solvation shell in

1 M LiTFSI-2 M $LiNO_3$-TEP is suggested to promote the Li^+ diffusion in this electrolyte formulation, thus increasing the diffusion coefficient (refer to Figure 1).

The ion pair formation for the selected compositions was further studied by Raman spectroscopy, focusing on the stretching modes of S−N−S and NO_3^- groups. As shown in Figure 2b, with the increase of LiTFSI concentration, the S−N−S stretching band of $TFSI^-$ located at 740 cm^{-1} gradually shifts to higher wavenumbers, indicating higher Li^+-$TFSI^-$ association, and thus decrease of the amount of free $TFSI^-$.[33] This is in agreement with the Density functional theory (DFT) results wherein it is also found that 2TEP-Li-TFSI becomes gradually the main solvation species in the electrolyte, accompanied by gradual disappearance of $(4TEP\text{-}Li)^+\cdots TFSI^-$ as the concentration of LiTFSI is increased (Figures S1−S3 and Figure 1b). In the $LiNO_3$-TEP system, the symmetric stretching band of NO_3^- at around 1040 cm^{-1} does not change significantly with the increase of $LiNO_3$ concentration, given the relatively uniform solvation structure in the $LiNO_3$-TEP system (Figure 1c and Figure S4), attributed to the strong Li---NO_3 pairing and efficient displacement of TEP from the solvation shell.[35] In the dual-salt electrolyte system, when compared to the 1 M LiTFSI-TEP and 2 $LiNO_3$-TEP parent systems, both the S−N−S stretching band of $TFSI^-$ and the symmetric stretching band of NO_3^- are slightly shifted to higher wavenumbers, demonstrating that the Li^+-$TFSI^-$ and Li^+-NO_3^- coordination has been enhanced by the combination of LiTFSI and $LiNO_3$. The complementary NMR and Raman results support thus the DFT analysis on

278 the particular cation-anion-solvent interactions and solvation structure in the dual-salt
279 electrolyte system.
280
281 *3.2. Solid-electrolyte interphase on Li metal*
282 An anion-rich solvation shell is expected to influence the dynamics and
283 composition of the SEI, thus, depth-dependent XPS characterization (Figure 3 and
284 Figure S10−S12) was conducted to analyze the composition of the SEI on Li metal
285 surface. Figure 3 displays the survey of the C 1s, F 1s and N 1s signals from the SEI
286 formed with 1 M LiTFSI-2 M $LiNO_3$-TEP and 3 M LiTFSI-TEP electrolytes. There are
287 significant differences between the two samples, with the main found in the N 1s
288 spectra. As shown in Figure 3c, the depth-dependent XPS survey of the SEI formed in
289 3 M LiTFSI-TEP reveals only two peaks located at 400 eV and 398 eV, assigned to
290 N−S and Li_3N species, respectively.[29, 36] In the 1 M LiTFSI-2 M $LiNO_3$-TEP
291 system, apart from the N−S and Li_3N species, an additional peak at 396 eV is revealed
292 upon SEI surface ablation, assigned to the ionically conductive LiN_xO_y derived from
293 the decomposition of $LiNO_3$.[29, 37, 38] From the C 1s (Figure 3a) and F 1s (Figure
294 3b) data, the surface chemical compositions for both electrolytes are similar, yet higher
295 amounts of inorganic compounds (i.e., LiF) can be observed for 1 M LiTFSI-2 M
296 $LiNO_3$-TEP. Furthermore, it is notable that whereas the outer layer of the SEI is rich in
297 organic species (e.g., C−F, N−S, etc.), these are nearly absent in the inner parts of the

SEI layer. This can be ascribed to the particular solvation structure altered by the introduction of $LiNO_3$, which can promote the complete decomposition of $TFSI^-$ anion to LiF.[29] As suggested in the previous studies,[39] the inorganic LiN_xO_y and LiF species can enhance the structural stability and ionic conductivity of the SEI film, thus effectively stabilizing the Li metal/electrolyte interface and facilitating a uniform and rapid deposition of Li. Thus, the combination of $LiNO_3$ and LiTFSI induces an SEI with compatible properties with the TEP solvent, primarily endowed by the abundance of inorganic LiN_xO_y and LiF species.

3.3. Electrochemical and Physico-chemical performances

The ionic conductivity of the selected 3 M electrolytes (1 M LiTFSI-2 M $LiNO_3$-TEP and 3 M LiTFSI-TEP) were measured at temperatures ranging from 20 °C to −70 °C and the data fitted to Vogel-Fulcher-Tammann model as shown in Figure S13. Table S1 lists the fitting parameters and calculated activation energy of 1 M LiTFSI-2 M $LiNO_3$-TEP and 3 M LiTFSI-TEP electrolytes.[40-42] As shown in Figure S14a, the ionic conductivity of 1 M LiTFSI-2 M $LiNO_3$-TEP electrolyte is systematically higher than that of the 3 M LiTFSI-TEP system, while considering that both have the same molarity in Li cation. Especially at −70 °C, one order of magnitude difference is measured (0.011 mS cm^{-1} vs. 0.001 mS cm^{-1}, respectively), pointing towards the potential benefits of 1 M LiTFSI-2 M $LiNO_3$-TEP electrolyte for low temperature

318 applications. The Li transference numbers (t_{Li+}) of the two electrolytes were also
319 determined (Figures S14b and S15, Table S2). Specifically, the t_{Li+} of 1 M LiTFSI-2 M
320 $LiNO_3$-TEP electrolyte is calculated to be 0.51 at 20 °C, two times higher than that of
321 the 3 M LiTFSI-TEP electrolyte (0.22). The viscosity of 1 M LiTFSI-2 M $LiNO_3$-TEP
322 electrolyte is 20.4 mPa·s at 30 °C, which allows faster wettability and impregnation of
323 the electrodes and separator, as well as enhance ionic conductivity (Figure S16, S17).
324 A wide electrochemical stability window of 1 M LiTFSI-2 M $LiNO_3$-TEP electrolyte
325 was also measured, making this formulation compatible with numerous cathode
326 electrode materials such as NCM and $LiFePO_4$ (LFP) (Figure S18).
327 TGA and DSC tests have been also conducted to analyse the thermal stability of
328 these electrolytes. As shown in Figure S19, the 1 M LiTFSI-2 M $LiNO_3$-TEP shows a
329 first decomposed step from 165 °C, and a loss of almost 50% of weight in this process,
330 which is due to the decomposition of nitrate anions into oxygen and nitrogen dioxide
331 [43]. After that, an endothermic peak appeared at ~ 290 °C in the DSC curve of 1 M
332 LiTFSI-2 M $LiNO_3$-TEP as well as the 3 M LiTFSI in TEP, indicating the phosphate-
333 based electrolyte starting decomposed. The TGA/DSC result shows that the $LiNO_3$ co-
334 salts will affect the thermal stability of the phosphate-based electrolyte to some extent,
335 especially in the first NO_3^- decomposition process. However, we should note that the 1
336 M LiTFSI-2 M $LiNO_3$-TEP still has better thermal stability than the common

commercial carbonate-based electrolyte as 1 M $LiPF_6$ in EC/DMC (Figure S19), which means that it can still be used as an electrolyte to improve battery safety performance.

The electrochemical performances of the two electrolyte systems were next studied in symmetrical Li||Li cells (Figure 4). At a current density of 0.25 mA cm^{-2} with a fixed capacity of 0.25 mAh cm^{-2}, the cells with 1 M LiTFSI-2 M $LiNO_3$-TEP exhibits a reversible and stable Li plating/stripping behavior over 200 cycles with only a small overpotential of 90 mV. On the contrary, the cells with 3 M LiTFSI-TEP consistently displayed faster and severe polarization (150 mV) and degradation over less than 20 cycles (Figure 4a). Even at higher current densities (0.5 mA cm^{-2}) and cutoff capacities (0.5 mAh cm^{-2}), the cell with 1 M LiTFSI-2 M $LiNO_3$-TEP provides considerably higher stability compared with 3 M LiTFSI-TEP system (150 vs 10 cycles, respectively; Figure S20).

Figure 4b displays the stability and the polarization curves for the two electrolyte systems at different current densities. With the current density increasing from 0.1 to 0.25 and to 0.5 mA cm^{-2}, the cell with 1 M LiTFSI-2 M $LiNO_3$-TEP shows minor increase of the overpotential of 40, 90, and 180 mV, respectively. Notably, when the current density is decreased to 0.1 mA cm^{-2}, the overpotential is returned to the initial value of 40 mV and keeps stable with further cycling. On the contrary, the cell with 3 M LiTFSI-TEP shows higher polarization, and failure at 0.5 mA cm^{-2}.

356 The electrochemical impedance spectroscopy (EIS) of the Li||Li cells with the two
357 electrolyte systems after several cycles was also conducted and results are shown in
358 Figure S21 and Table S3. With cycling, both the Rs (Ohmic resistance) and Rint
359 (interfacial resistance) of the cell with 3 M LiTFSI-TEP increase (Figure S21a), a clear
360 indication of unstable and excess SEI growth (either mechanically unstable, soluble, or
361 porous and permeable to electrolyte).[44] Oppositely, the impedance of the cell with 1
362 M LiTFSI-2 M $LiNO_3$-TEP stabilizes after the 1st cycle and no significant changes with
363 further cycling are noted (Figure S21b and Table S3), indicating increased interfacial
364 stability, ascribed to the stabilizing effect of LiF-LiN_xO_y-rich SEI on Li metal surface.
365 To further confirm this, the morphology of the Li metal anodes after cycling was
366 analyzed by optical inspection and scanning electron microscopy (SEM). As shown in
367 Figure 4c-e, after cycling at a current density of 0.25 mA cm^{-2} with a cut-off capacity
368 of 0.25 mAh cm^{-2} in 1 M LiTFSI-2 M $LiNO_3$-TEP for 10 cycles, the surface of the Li
369 anode is smooth, dendrite-free and keeps the shiny metallic luster, whereas for the 3 M
370 LiTFSI-TEP based cell cycled under similar conditions, the surface is rough and
371 exhibits a large number of dendrites and "dead Li" (Figure 4f-h).
372 Finally, NCM523||Li cells were assembled to evaluate the potential application of
373 1 M LiTFSI-2 M $LiNO_3$-TEP electrolyte in Li metal batteries. As shown in Figures 5a
374 and b, the NCM523||Li cell with 1 M LiTFSI-2 M $LiNO_3$-TEP provides prolonged
375 cycling for over 120 cycles with a capacity retention of more than 98% at a current

density of 88.5 mA g^{-1} (C/2). Even at higher current density of 360 mA g^{-1} (2C), the cell can still retain a reversible capacity of 78 mAh g^{-1}, whereas the cell with 3 M LiTFSI-TEP failed to deliver any capacity at a same current density (Figure 5c). Further, we also investigated the influence of temperature on the performance of the two electrolyte systems in NCM523||Li cell configuration. As displayed in Figure 5d, both electrolytes provide comparable performances at 20 °C, with a discharge capacity of nearly 160 mAh g^{-1} for both cells. When cycled at 0 °C, no capacity was possible to recover from the 3 M LiTFSI-TEP cell, while with 1 M LiTFSI-2 M $LiNO_3$-TEP, 120 mAh g^{-1} (70% of the nominal capacity) was retained. Essential, even at temperatures as low as −40 °C, this cell retained a capacity of 40 mAh g^{-1}, highlighting the wide operating temperature range of the dual-salt electrolyte. Despite further improvements still required, for instance consider the possible continuous consumption of nitrate species at the electrodes, these results consolidate the ability of the dual-salt electrolyte systems to improve the performance of Li metal-based batteries (e.g., NCM523||Li) used with safe and flame-retardant electrolytes, factors attributed to the particular solvation structure inducing the formation of an anion-derived SEI with high quality and high ionic conductivity.

4. Conclusions

A dual-salt organic phosphate-based electrolyte comprising $LiNO_3$ and LiTFSI in TEP is shown suitable to address the interfacial compatibility issues between phosphate-based electrolyte and Li metal anode at moderate Li-cation concentrations. The experimental results and DFT calculations demonstrate that the dual-salt electrolyte system based on 1 M LiTFSI-2 M $LiNO_3$ in TEP develops a solvation structure with mixed anions (NO_3^- and $TFSI^-$) pairing through Li^+ in the primary solvation shell, which promotes the formation of a robust anion-derived SEI. Such an SEI film contains essentially inorganic species (e.g., LiF, Li_3N and LiN_xO_y, etc.) as compared to the single-salt electrolyte system, with thus significantly improved interfacial compatibility. Consequently, when the electrolyte of 1 M LiTFSI-2 M $LiNO_3$ in TEP is used, the NCM523||Li cells attain high initial capacities (178 mAh g^{-1}), good cycling stability (98% after 130 cycles) as well as higher rate capability and low temperature performances as compared to single salt constituent equivalent formulations. This work not only provides an effective electrolyte design strategy towards the incompatibility problem between phosphate-based electrolyte and Li metal anode, but also provides guidelines on the combined computational and experimental rationale design of electrolytes for next generation batteries with improved performances. The dual salt approach may be applied to other high concentration electrolytes such as water in salt electrolyte to alter the electrolyte solvation structure

to generate a robust anion-derived SEI even at relatively low/medium concentration [45].

Acknowledgements

The authors acknowledge China Scholarship Council, F.R.S.-FNRS through grant No° - F.4552.21 – DEMIST, CF-ARC grant (18/23-093) MICROBAT, as well as partial support from European Research Council (ERC) under the European Union's Horizon 2020 research and innovation program (grant agreement no. 770870) and the Projects of National Natural Science Foundation of China (U1805254, U1705255, 21773192, 22072117) for financial support.

Declaration of competing interest

There are no conflicts to declare.

Data availability

The datasets generated and analyzed during the current study are available from the corresponding author upon reasonable request.

References

[1] N. Nitta, F. Wu, J.T. Lee, G. Yushin, Materials today, 18 (2015) 252-264.

[2] Y. Tian, G. Zeng, A. Rutt, T. Shi, H. Kim, J. Wang, J. Koettgen, Y. Sun, B. Ouyang, T. Chen, Chemical

reviews, 121 (2020) 1623-1669.
[3] E. Fan, L. Li, Z. Wang, J. Lin, Y. Huang, Y. Yao, R. Chen, F. Wu, Chemical reviews, 120 (2020) 7020-7063.
[4] Q. Zhu, J. Wang, X. Liu, N. Ebejer, D. Rambabu, A. Vlad, Angewandte Chemie International Edition, 59 (2020) 16579-16586.
[5] R. Rupp, A. Vlad, Journal of The Electrochemical Society, 166 (2019) A3122.
[6] J. Wang, Y. Yamada, K. Sodeyama, E. Watanabe, K. Takada, Y. Tateyama, A. Yamada, Nature Energy, 3 (2018) 22-29.
[7] Q. Zheng, Y. Yamada, R. Shang, S. Ko, Y.-Y. Lee, K. Kim, E. Nakamura, A. Yamada, Nature Energy, 5 (2020) 291-298.
[8] J. Chen, Z. Yang, G. Liu, C. Li, J. Yi, M. Fan, H. Tan, Z. Lu, C. Yang, Energy Storage Materials, 25 (2020) 305-312.
[9] H. Zhang, J. Luo, M. Qi, S. Lin, Q. Dong, H. Li, N. Dulock, C. Povinelli, N. Wong, W. Fan, Angewandte Chemie International Edition, 60 (2021) 19183-19190.
[10] R. Rupp, B. Caerts, A. Vantomme, J. Fransaer, A. Vlad, The journal of physical chemistry letters, 10 (2019) 5206-5210.
[11] G. Yang, Y. Song, Q. Wang, L. Zhang, L. Deng, Materials & Design, 190 (2020) 108563.
[12] J. Fu, Y. Xu, L. Dong, L. Chen, Q. Lu, M. Li, X. Zeng, S. Dai, G. Chen, L. Shi, Chemical Engineering Journal, 405 (2021) 126942.
[13] J. Hu, Z. Yao, K. Chen, C. Li, Energy Storage Materials, 28 (2020) 37-46.
[14] L. Xia, H. Miao, C. Zhang, G.Z. Chen, J. Yuan, Energy Storage Materials, 38 (2021) 542-570.
[15] H.K. Bezabh, S.-F. Chiu, T.M. Hagos, M.-C. Tsai, Y. Nikodimos, H.G. Redda, W.-N. Su, B.J. Hwang, Journal of Power Sources, 494 (2021) 229760.
[16] X. Cao, X. Ren, L. Zou, M.H. Engelhard, W. Huang, H. Wang, B.E. Matthews, H. Lee, C. Niu, B.W. Arey, Nature Energy, 4 (2019) 796-805.
[17] Z. Zeng, V. Murugesan, K.S. Han, X. Jiang, Y. Cao, L. Xiao, X. Ai, H. Yang, J.-G. Zhang, M.L. Sushko, Nature Energy, 3 (2018) 674-681.
[18] P. Zhai, L. Liu, X. Gu, T. Wang, Y. Gong, Advanced Energy Materials, 10 (2020) 2001257.
[19] K. Takada, Y. Yamada, A. Yamada, ACS applied materials & interfaces, 11 (2019) 35770-35776.
[20] Z. Wang, F. Qi, L. Yin, Y. Shi, C. Sun, B. An, H.M. Cheng, F. Li, Advanced Energy Materials, 10 (2020) 1903843.
[21] X. Shen, H. Ji, J. Liu, J. Zhou, C. Yan, T. Qian, Energy Storage Materials, 24 (2020) 426-431.
[22] Y. Dong, N. Zhang, C. Li, Y. Zhang, M. Jia, Y. Wang, Y. Zhao, L. Jiao, F. Cheng, J. Xu, ACS Applied Energy Materials, 2 (2019) 2708-2716.
[23] Y. Yamada, J. Wang, S. Ko, E. Watanabe, A. Yamada, Nature Energy, 4 (2019) 269-280.
[24] J. Kalhoff, G.G. Eshetu, D. Bresser, S. Passerini, ChemSusChem, 8 (2015) 2154-2175.
[25] L.-N. Wu, J. Peng, Y.-K. Sun, F.-M. Han, Y.-F. Wen, C.-G. Shi, J.-J. Fan, L. Huang, J.-T. Li, S.-G. Sun, ACS applied materials & interfaces, 11 (2019) 18504-18510.
[26] Y. Liu, X. Qin, D. Zhou, H. Xia, S. Zhang, G. Chen, F. Kang, B. Li, Energy Storage Materials, 24 (2020) 229-236.

[27] S. Chen, P. Sun, B. Sun, J. Humphreys, P. Zou, K. Xie, S. Tao, Energy Storage Materials, 37 (2021) 598-608.
[28] X.-Q. Zhang, X. Chen, L.-P. Hou, B.-Q. Li, X.-B. Cheng, J.-Q. Huang, Q. Zhang, ACS Energy Letters, 4 (2019) 411-416.
[29] J. Fu, X. Ji, J. Chen, L. Chen, X. Fan, D. Mu, C. Wang, Angewandte Chemie, 132 (2020) 22378-22385.
[30] B. Ernould, L. Sieuw, G. Barozzino-Consiglio, J.-F. Gohy, A. Vlad, ACS Applied Energy Materials, 2 (2019) 7879-7885.
[31] Z. Zeng, V. Murugesan, K.S. Han, X. Jiang, Y. Cao, L. Xiao, X. Ai, H. Yang, J.-G. Zhang, M.L. Sushko, Nature Energy, 3 (2018) 674-681.
[32] C.M. Burke, V. Pande, A. Khetan, V. Viswanathan, B.D. McCloskey, Proceedings of the National Academy of Sciences, 112 (2015) 9293-9298.
[33] J. Ming, Z. Cao, W. Wahyudi, M. Li, P. Kumar, Y. Wu, J.-Y. Hwang, M.N. Hedhili, L. Cavallo, Y.-K. Sun, Acs Energy Letters, 3 (2018) 335-340.
[34] M. Okoshi, C.-P. Chou, H. Nakai, The Journal of Physical Chemistry B, 122 (2018) 2600-2609.
[35] J.-Y. Yu, Y. Zhang, S.-H. Tan, Y. Liu, Y.-H. Zhang, The Journal of Physical Chemistry B, 116 (2012) 12581-12589.
[36] H. Xu, Y. Li, A. Zhou, N. Wu, S. Xin, Z. Li, J.B. Goodenough, Nano letters, 18 (2018) 7414-7418.
[37] S.J. Tan, J. Yue, X.C. Hu, Z.Z. Shen, W.P. Wang, J.Y. Li, T.T. Zuo, H. Duan, Y. Xiao, Y.X. Yin, Angewandte Chemie, 131 (2019) 7884-7889.
[38] Z. Li, C. Song, P. Dai, X. Wu, S. Zhou, Y. Qiao, L. Huang, S.-G. Sun, Nano Letters, 22 (2022) 815-821.
[39] S. Liu, X. Ji, N. Piao, J. Chen, N. Eidson, J. Xu, P. Wang, L. Chen, J. Zhang, T. Deng, Angewandte Chemie International Edition, 60 (2021) 3661-3671.
[40] F. Croce, M.L. Focarete, J. Hassoun, I. Meschini, B. Scrosati, Energy & Environmental Science, 4 (2011) 921-927.
[41] G. Gu, S. Bouvier, C. Wu, R. Laura, M. Rzeznik, K. Abraham, Electrochimica acta, 45 (2000) 3127-3139.
[42] X. Fan, X. Ji, L. Chen, J. Chen, T. Deng, F. Han, J. Yue, N. Piao, R. Wang, X. Zhou, Nature Energy, 4 (2019) 882-890.
[43] Meng, J.; Pan, Y.; Ran, Z.; Li, Y.; Jiang, J.; Wang, Q.; Jiang, J., Journal of Loss Prevention in the Process Industries 2021, 72, 104562.
[44] X.-D. Lin, Y. Gu, X.-R. Shen, W.-W. Wang, Y.-H. Hong, Q.-H. Wu, Z.-Y. Zhou, D.-Y. Wu, J.-K. Chang, M.-S. Zheng, Energy & Environmental Science, 14 (2021) 1439-1448.
[45] Xie, J.; Liang, Z.; Lu, Y.-C., Molecular crowding electrolytes for high-voltage aqueous batteries. Nature materials 2020, 19 (9), 1006-1011.

Figures and Captions.

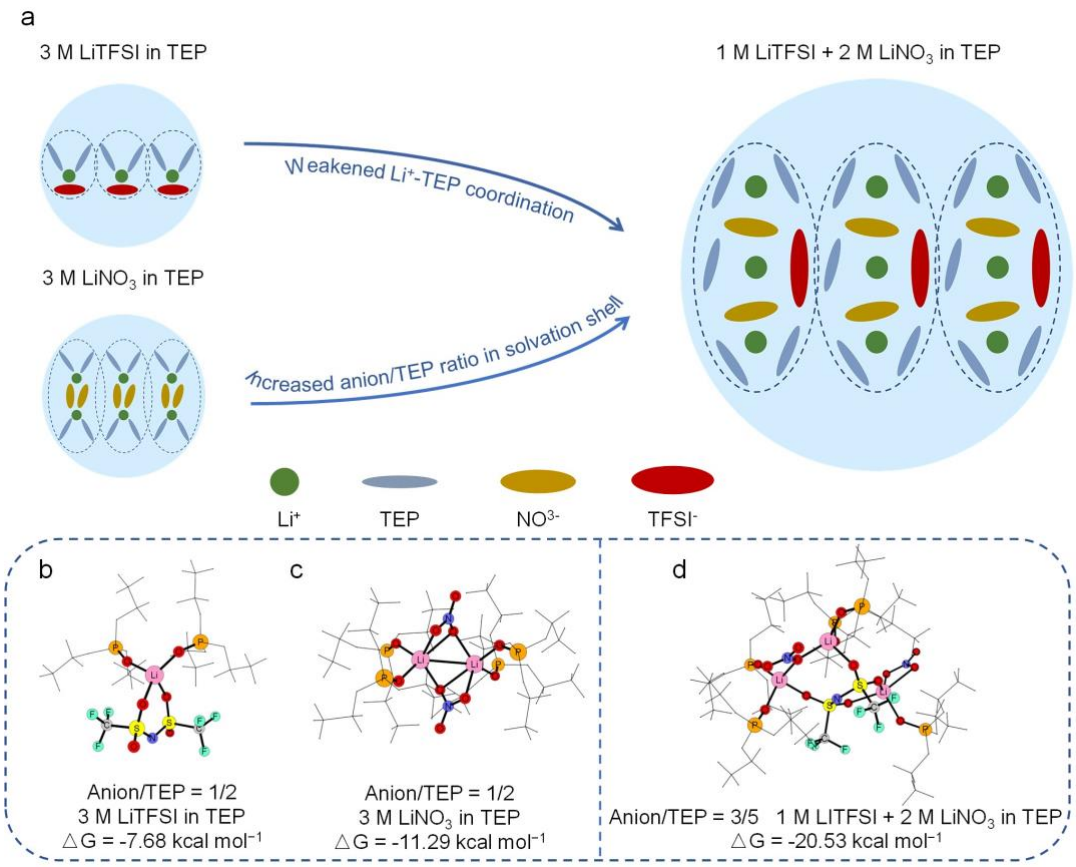

Figure 1. (a) Schematic representation of the ion pair aggregates present in the main electrolyte formulations studied in this work, all for a total concentration of 3 M in Li cation. **(b−d)** DFT optimized solvation structures of 3 M LiTFSI-TEP **(b)**, 3 M $LiNO_3$-TEP **(c)** and 1 M LiTFSI-2 M $LiNO_3$-TEP **(d)** electrolytes at 298 K.

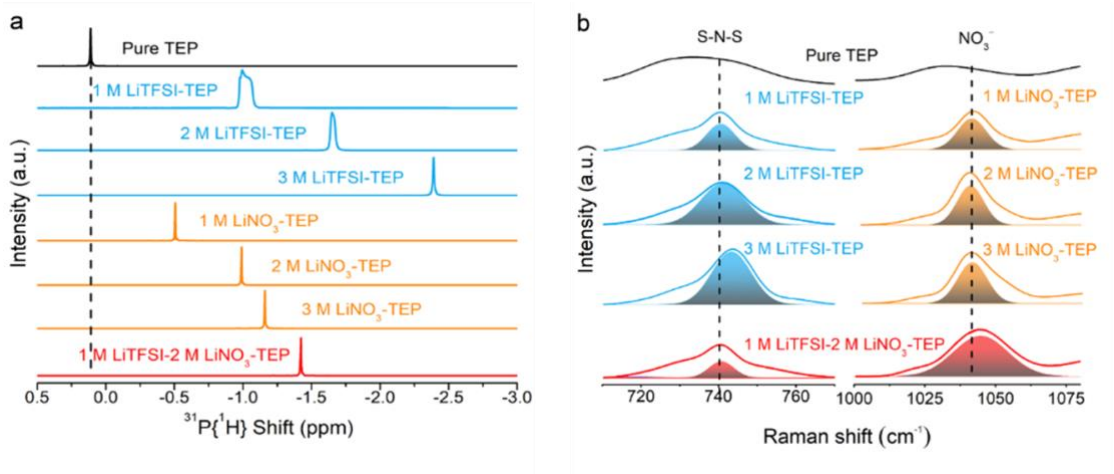

Figure 2. The ^{31}P NMR **(a)** and Raman **(b)** spectra of the electrolytes containing different concentrations of LiTFSI , $LiNO_3$, or mixed salt composition in TEP solvent.

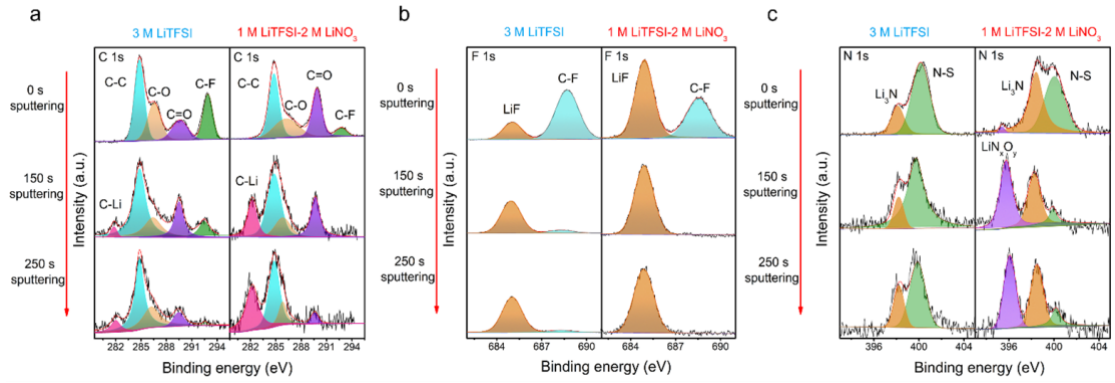

Figure 3. The depth-dependent XPS survey of C 1s **(a)**, F 1s **(b)** and N 1s **(c)** signals of the SEI films formed on Li anode after 10 cycles in 3 M LiTFSI-TEP and in 1 M LiTFSI-2 M $LiNO_3$-TEP electrolytes at current density of 0.25 mA cm^{-2}.

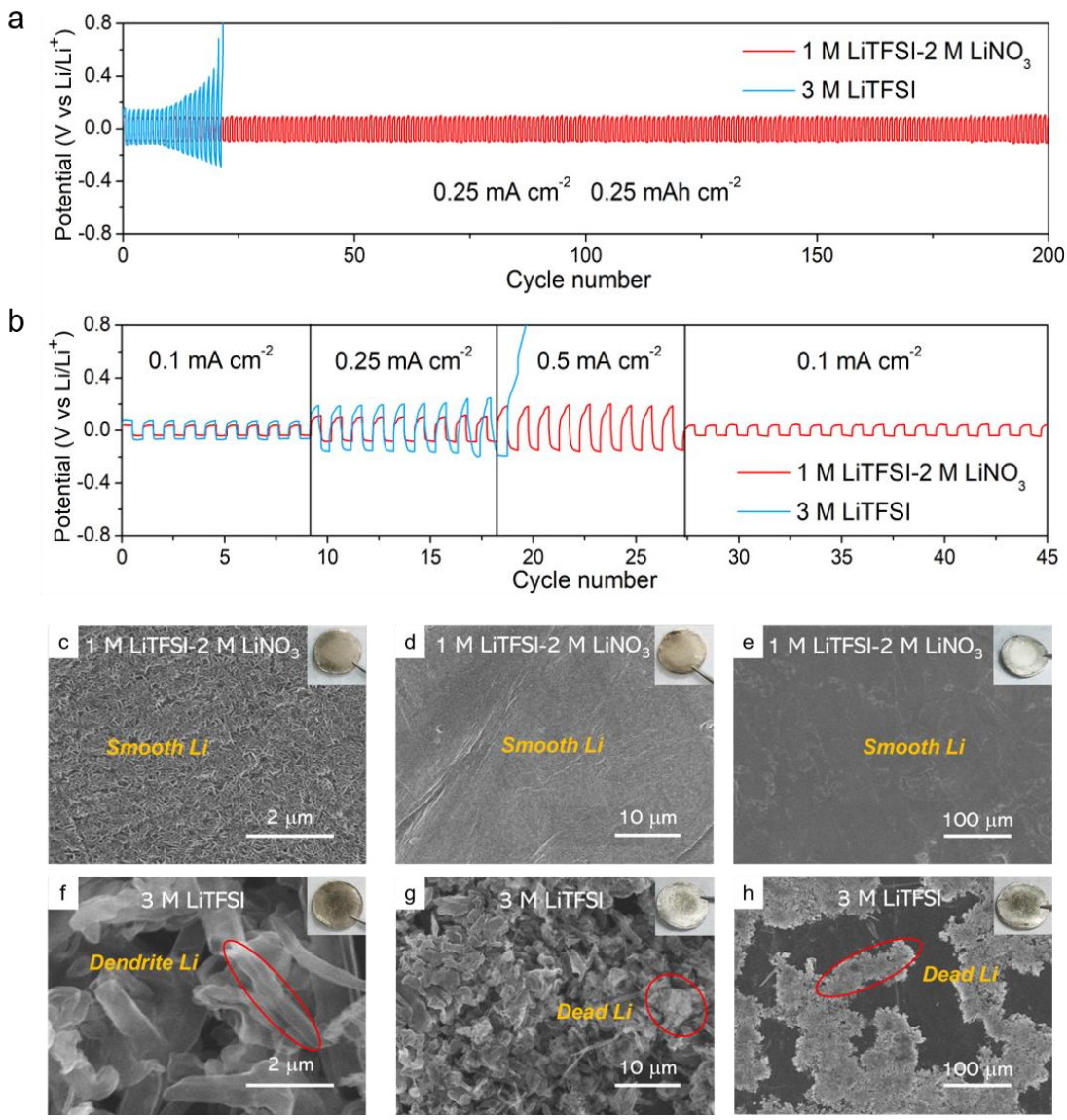

Figure 4. Electrochemical performances in symmetric Li−Li cells with 3 M LiTFSI and 1 M LiTFSI-2 M $LiNO_3$ in TEP electrolytes **(a)** cycled at current density of 0.25 mA cm^{-2} with the two electrolytes, and **(b)** at variable current densities. Optical (insets) and SEM images at different magnifications of Li metal chips after 10 cycles in **(c-e)** 1 M LiTFSI-2 M $LiNO_3$-TEP and **(f-h)** 3 M LiTFSI-TEP electrolyte.

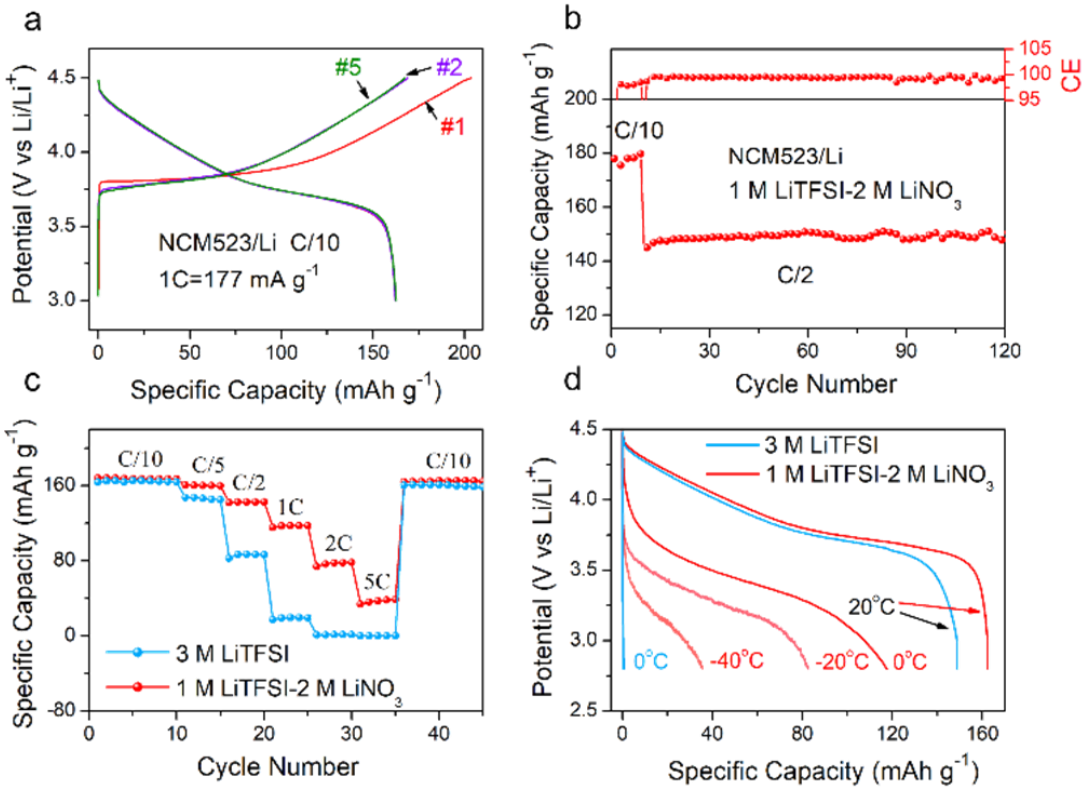

Figure 5. Electrochemical performances of NCM523||Li cells. Galvanostatic charge–discharge profiles **(a)** and cycling performance **(b)** of the NCM523||Li cell with 1 M LiTFSI-2 M $LiNO_3$-TEP electrolyte at a current density of 88.5 mA g^{-1} Note: the cell was activated at 17.7 mA g^{-1} in the initial 5 cycles before being operated at 88.5 mA g^{-1}. Top inset to panel **b** - the Coulombic efficiency of the respective cell. **(c)** Rate performance of the NCM523||Li cells with 3 M LiTFSI-TEP and 1 M LiTFSI-2 M $LiNO_3$-TEP electrolytes. **(d)** Discharge profiles of the NCM523||Li cells with 3 M LiTFSI-TEP and 1 M LiTFSI-2 M $LiNO_3$-TEP electrolytes at different temperatures (Discharge current density: 35.4 mA g^{-1}).